ELSEVIER

NeuroImage

www.elsevier.com/locate/ynimg
NeuroImage 31 (2006) 125 – 138

Estimating linear cortical magnification in human primary visual cortex via dynamic programming

Anqi Qiu,[a,b,*] Benjamin J. Rosenau,[c] Adam S. Greenberg,[c] Monica K. Hurdal,[d] Patrick Barta,[a,e,f] Steven Yantis,[c] and Michael I. Miller[a,e]

[a]*Center for Imaging Science, Johns Hopkins University, Baltimore, MD 21218, USA*
[b]*Department of Electrical and Computer Engineering, Johns Hopkins University, Baltimore, MD 21218, USA*
[c]*Department of Psychological and Brain Sciences, Johns Hopkins University, Baltimore, MD 21218, USA*
[d]*Department of Mathematics, Florida State University, Tallahassee, FL 32306, USA*
[e]*Department of Biomedical Engineering, Johns Hopkins University, Baltimore, MD 21218, USA*
[f]*Department of Psychiatry, Johns Hopkins University School of Medicine, Baltimore, MD 21205, USA*

Received 16 May 2005; revised 22 November 2005; accepted 28 November 2005
Available online 8 February 2006

Human primary visual cortex is organized retinotopically, with adjacent locations in cortex representing adjacent locations on the retina. The spatial sampling in cortex is highly nonuniform: the amount of cortex devoted to a unit area of retina decreases with increasing retinal eccentricity. This sampling property can be quantified by the linear cortical magnification factor, which is expressed in terms of millimeters of cortex per degree of visual angle. In this paper, we present a new method using dynamic programming and fMRI retinotopic eccentricity mapping to estimate the linear cortical magnification factor in human primary visual cortex (V1). We localized cortical activity while subjects viewed each of seven stationary contrast- reversing radial checkerboard rings of equal thickness that tiled the visual field from 1.62 to 12.96 degrees of eccentricity. Imaging data from all epochs of each ring were contrasted with data from fixation epochs on a subject-by-subject basis. The resulting *t* statistic maps were then superimposed on a local coordinate system constructed from the gray/white matter boundary surface of each individual subject's occipital lobe, separately for each ring. Smoothed maps of functional activity on the cortical surface were constructed using orthonormal bases of the Laplace–Beltrami operator that incorporate the geometry of the cortical surface. This allowed us to stably track the ridge of maximum activation due to each ring via dynamic programming optimization over all possible paths on the cortical surface. We estimated the linear cortical magnification factor by calculating geodesic distances between activation ridges on the cortical surface in a population of five normal subjects. The reliability of these estimates was assessed by comparing results based on data from one quadrant to those based on data from the full hemifield along with a split-half reliability analysis.

Keywords: Retinotopic mapping; Linear cortical magnification; Laplace–Beltrami operator; Dynamic programming

Introduction

Studies of visual field loss following cortical lesions have shown that human primary visual cortex is retinotopically organized: adjacent neurons in the visual cortex correspond to adjacent locations in the visual field (Inouye, 1909; Holmes, 1918; Horton and Hoyt, 1991). The center of the visual field occupies the occipital pole, while the periphery is mapped to more anterior parts of the occipital cortex, forming a retinotopic eccentricity map. Within primary visual cortex (area V1), as one moves from the V1/V2d (dorsal V2) border through the calcarine sulcus to the V1/V2v (ventral V2) border, the representation of the visual field sweeps from the lower vertical meridian through the horizontal meridian to the upper vertical meridian, forming a retinotopic polar angle map. Such mapping of retinal space to cortical space is referred to as retinotopy. The spatial sampling of the visual cortex is highly nonuniform: the cortical representation of the fovea is much larger than that of the periphery. Daniel and Whitteridge (1961) first used the term linear cortical magnification factor to refer to the quantitative relationship between visual cortex and visual field in terms of the number of millimeters of visual cortex representing one degree of visual field at any given eccentricity.

Anatomical magnetic resonance imaging and functional magnetic resonance imaging (MRI, fMRI) have made it possible to precisely delineate the retinotopic organization of human visual

* Corresponding author. Center for Imaging Science, 301 Clark Hall, 3400 N. Charles Street, Baltimore, MD 21218, USA. Fax: +1 410 516 4594.
E-mail address: anqi@cis.jhu.edu (A. Qiu).
Available online on ScienceDirect (www.sciencedirect.com).

1053-8119/$ - see front matter © 2005 Elsevier Inc. All rights reserved.
doi:10.1016/j.neuroimage.2005.11.049

cortex and quantitatively investigate the linear cortical magnification factor, especially in area V1 (Schneider et al., 1993; Engel et al., 1994; Sereno et al., 1995; Engel et al., 1997; Tootell et al., 1997; DeYoe et al., 1996; Duncan and Boynton, 2003). These techniques open clinical possibilities to study visual pathology and develop new strategies for rehabilitation (Baseler et al., 1999; Morland et al., 2001; Sunness et al., 2004; Baker et al., 2005). The following broad steps are involved in fMRI retinotopic mapping using phase-encoding stimuli (expanding ring and rotating wedge, or stationary rings and wedges) (Schneider et al., 1993; Engel et al., 1994; Shipp et al., 1995; Tootell et al., 1995; Sereno et al., 1995): the reconstruction of the highly convoluted cortical surface, including classification of tissues (Dale and Sereno, 1993; Well et al., 1996; Kapur et al., 1996; Thompson et al., 1996; Teo et al., 1997; Dale et al., 1999; Miller et al., 2000; Joshi et al., 1999; Ratnanather et al., 2001; Xu et al., 1999; Harris et al., 1999; MacDonald et al., 2000; Fischl et al., 2001; Zhang et al., 2000, 2001a,b; Fischl et al., 2002; Shattuck and Leahy, 2001), topological correction of the surface mesh (Shattuck et al., 2001; Han et al., 2001, 2002), and unfolding the cortical surface into a 2D plane (Thompson et al., 1996; Van Essen et al., 1998; Toga, 1999; Angenent et al., 1999; Fischl et al., 1999a,b; Hurdal et al., 1999; Lewis and Van Essen, 2000; Collins and Stephenson, 2003b); analysis of the fMRI response (Engel et al., 1997; Andrade et al., 2001; Warnking et al., 2002); smoothing of functional data over the cortical surface (Andrade et al., 2001; Warnking et al., 2002); localization of functional response to phase-encoded stimuli; and, finally, measurement of the linear cortical magnification factor (Sereno et al., 1995; Engel et al., 1997; Duncan and Boynton, 2003).

Although many fMRI retinotopic mapping studies in human primary visual cortex have been carried out in the last decade, there is no generally-accepted consensus about how to smooth functional data over the cortical surface while taking the cortical geometry into account. Furthermore, no methods for automatically delimiting the boundaries of V1 using fMRI have been generally accepted by the scientific community.

In this paper, we present all steps necessary for fMRI retinotopic mapping analysis and linear cortical magnification factor estimation in human primary visual cortex, from fMRI experimental design and anatomical MRI analysis to quantitative measurement of the linear cortical magnification. We use methods proposed by our own group and others for stimulus design, functional volume-based analysis, anatomical MRI segmentation, and unfolding the cortical surface. We present new methods for associating functional volume data with the cortical surface, smoothing functional data on the cortical surface using the geometric characteristics of the cortical surface expressed via orthonormal bases of the Laplace–Beltrami operator, automatically defining the V1 boundaries and tracking ridges of maximum activation evoked by stationary contrast-reversing rings via dynamic programming optimization, and measuring the linear cortical magnification factor in human primary visual cortex. We report results of the linear cortical magnification factor estimation in the left and right primary visual cortices in a population of five normal subjects. Finally, we test the multirun reliability of the estimates by comparing them based on the set of all odd- or even-numbered fMRI runs with estimates based on all fMRI runs and the spatial reliability of the estimates by comparing estimates based on data limited to the upper or lower quadrant in each visual hemifield with estimates based on the entire hemifield.

Methods

Functional MRI analysis

Acquisition

Functional MRI was performed using a Philips Intera 3.0 T scanner located at the F. M. Kirby Research Center for Functional Brain Imaging at the Kennedy Krieger Institute, Baltimore, MD. All images were acquired using a SENSE parallel imaging head coil.

We used single-shot echo-planar imaging (EPI) of 23 ascending 2 mm (no gap) axial-oblique slices with a field of view of 128 mm^2 and a 64 × 64 matrix allowing partial-brain coverage at high resolution (2 mm^3). Slices were positioned so as to maximally cover the occipital lobe on a subject-by-subject basis. Volumes were acquired every 2000 ms with a TE of 30 ms and a flip angle of 70°.

Visual stimuli and paradigm

Subjects were scanned while they viewed retinotopic mapping stimuli (stationary contrast-reversing rings and wedges). Each subject observed four runs (298 s per run) of a V1 localizer and 9–10 runs (272 s per run) of an eccentricity mapping paradigm during a singles scanning session. Visual stimulation was accomplished using in-house software written in C++ and projected on a screen at the head of the scanner bore using an Epson PowerLite 7600p projector fit with a custom lens (Buhl Optical, Pittsburgh, PA). Subjects viewed the screen via a first-surface mirror mounted on the head coil and were instructed to fixate the central fixation disk during all runs. Head stability was maintained with a bite bar custom-fitted for each subject.

Fig. 1a illustrates the V1 localizer paradigm. The V1 localizer consisted of two wedges, each subtending 60° of polar angle and composed of a radial black and white checkerboard reversing contrast at 8 Hz on a gray background. The wedges alternated between horizontal and vertical orientations every 18 s. A white fixation disk was displayed in the center of the screen where the wedges met. At the end of each run, subjects observed 10 s of the fixation disk without the wedges.

Fig. 1b demonstrates the eccentricity mapping stimuli. The eccentricity mapping paradigm consisted of seven equal-width annular rings that completely tiled visual space from 1.62 to 12.96 degrees of eccentricity. Each ring was 1.62° of visual angle in width; the mean of the inner and outer radii of the seven rings were as follows: 2.43, 4.05, 5.67, 7.29, 8.91, 10.53, and 12.15 degrees of eccentricity. The size of each check sequentially increased from the innermost ring to the outmost ring to improve the strength of the periphery activation and ensure that each ring had identical width. The rings were composed of an 8 Hz contrast-reversing black and white radial checkerboard. Rings were displayed for 16 s at a time, twice each per run, counter-balanced such that no ring was displayed twice before all had been displayed once and no ring was immediately followed by a spatially adjacent ring. A 0.27° radius disk divided into four quadrants (two black, two white; reversing contrast at 4 Hz) was randomly alternated with a white disk at fixation in order to provide a task to control subjects' attentional state; subjects held down a button in each hand during periods in which the fixation disk contained the contrast reversing stimulus. All rings were displayed on a gray background. Each run began and ended with 16 s periods of fixation without a ring stimulus, and

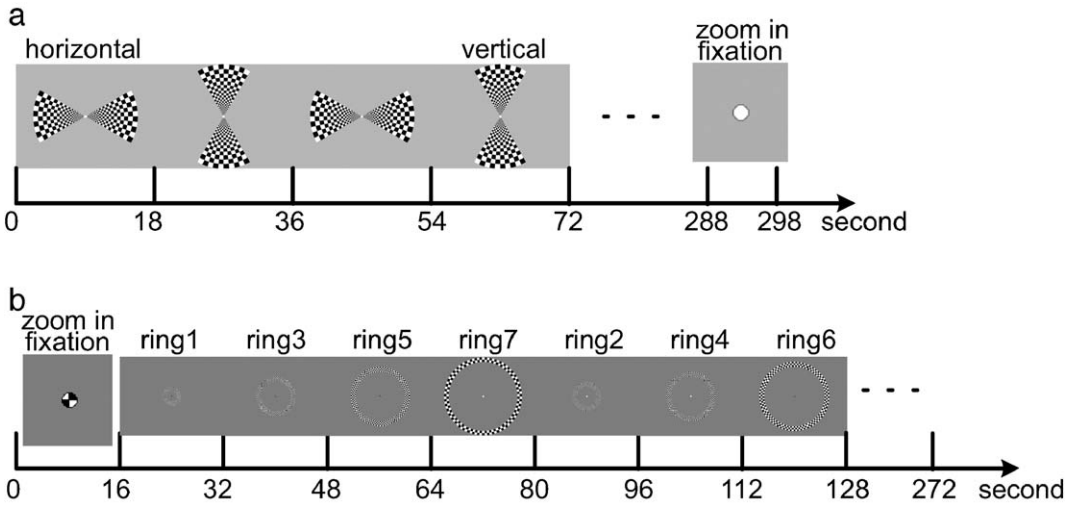

Fig. 1. Experimental design. Panel a illustrates the V1-localizer experiment. The horizontal and vertical meridia alternate every 18 s. At the end of each run, the subject observes 10 s of fixation-only. Panel b demonstrates the eccentricity experiment. Seven equal-width annular rings that tile space from 1.62 to 12.96° are displayed for 16 s at a time. Each ring is displayed twice per run. At the beginning, middle, and end of every run, the subject observes fixation-only for 16 s.

contained a third fixation period between the first and second repetitions of the set of seven rings.

Preprocessing and volume-based functional data analysis

Functional data were preprocessed using Brainvoyager (Brain Innovation B.V., Maastricht, the Netherlands). Preprocessing steps included: slice acquisition time correction, within-run motion correction, temporal high-pass filtering (1st–3rd order components), and temporal low-pass filtering (removing frequencies above approximately 2 cycles per stimulus block, using the shortest block in the run when a run contained blocks of multiple durations). One functional volume for each subject was manually aligned to the structural image; this transformation was then applied to all volumes in all runs.

All analysis was performed separately for each subject. For each subject, all runs of each type were normalized using a *z*-transform and then concatenated. Stimulation and fixation blocks were modeled by boxcar functions convolved with a canonical hemodynamic response function (Friston et al., 1994). For each run type, contrasts between relevant stimulus types (V1 localizer: horizontal meridian vs. vertical meridian; eccentricity stimulus: each ring individually vs. fixation) were used to generate unthresholded *t* statistic maps.

Anatomical MRI analysis

Acquisition

Whole-brain high resolution 3D structural MRI images were acquired using a T1 weighted MPRAGE sequence with a TR of 8.1 ms, TE of 3.8 ms, flip angle of 8°, coronal slice acquisition, time between inversions of 3 s, inversion time of 850 ms, and an isotropic resolution of 1 mm. A SENSE head coil was used during the acquisition.

Segmentation, surface generation, and conformal map

A 3D region of interest (ROI) subvolume encompassing the occipital lobe was defined manually for each of the two hemispheres in each subject (e.g., Fig. 2a). The ROI was delimited in the sagittal view in Robb et al. (1989) and is shown by white lines in Fig. 2a. A Bayesian segmentation using the expectation-maximization algorithm to fit the compartmental statistics was used to label voxels in the subvolume as gray matter (GM), white matter (WM), or cerebrospinal fluid (CSF) (Joshi et al., 1999; Miller et al., 2000). The segmentation accuracy of this method has been validated in various subregions of the brain in past studies (Ratnanather et al., 2001, 2004). Surfaces were generated at the GM/WM interface (the blue contour in Fig. 2a) using a topology-correction method and a connectivity-consistent isosurface algorithm (Han et al., 2001, 2002). The topology-correction method was applied to a binarized subvolume according to the gray and white intensity threshold to remove all handles of the WM object (Han et al., 2002). The connectivity-consistent isosurface algorithm is used to extract the isosurface of the edited image to guarantee that the extracted isosurface has the same topology as the object surface in the binarized image (Han et al., 2001). Finally, the portion of the surface to be unfolded was defined by one manual cut approximately parallel to the parieto-occipital sulcus (Fig. 2b) on the cortical surface.

For visualization purposes, the cortical surface was bijectively mapped into the 2D plane via a conformal mapping algorithm (Hurdal et al., 1999; Collins and Stephenson, 2003a). Such maps can be displayed in geometries of constant curvature: the Euclidean and hyperbolic planes, and the sphere. In this paper, maps on the hyperbolic plane were used to visualize functional activation due to the fact that the visual cortical surface on the hyperbolic plane can be represented by the unit disc. The unit disc is a natural representation for the visual cortex since the visual field is usually represented by a disc as well (Fig. 2d).

Fig. 2 illustrates these anatomical MRI analysis steps sequentially from panel (a) to panel (d) and shows anatomical landmarks on the visual cortical surface and its planar map. Critically, all measurements reported in this paper were carried out in the intrinsic coordinate system of the cortical surface and the results are shown on the planar map for ease of visualization only. The bijection to the planar map does not preserve the geodesic distance.

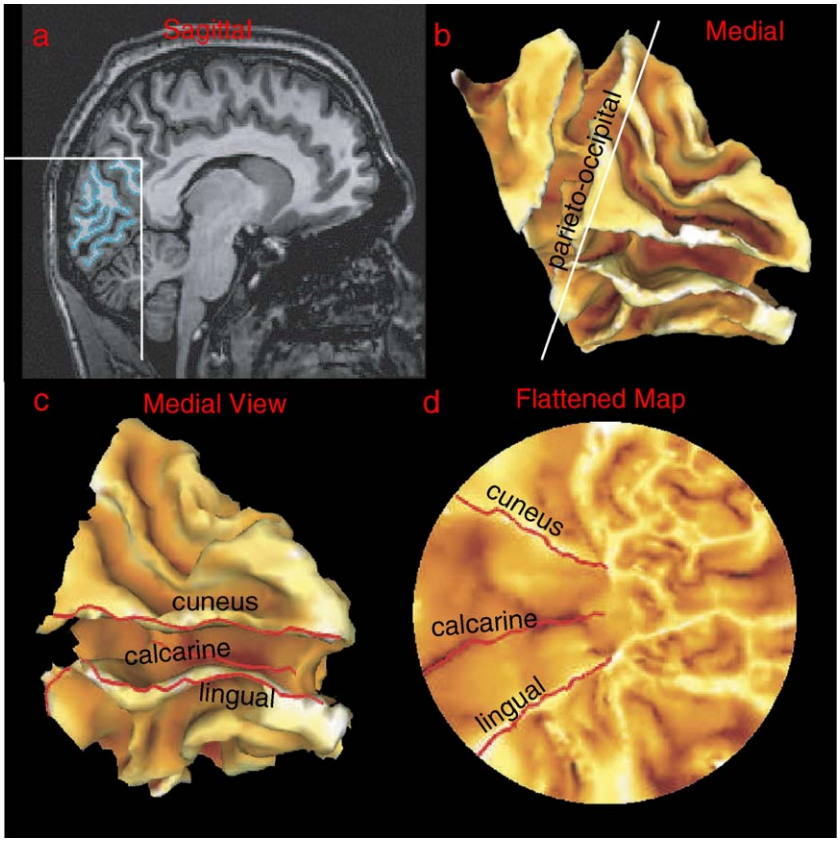

Fig. 2. Anatomical MRI analysis. (a) Sagittal slice in the MRI volume. The white lines delineate the region of interest, and the blue contour indicates the location of the GM/WM interface. (b) Right occipital lobe. The cut is delimited by the white line parallel to the parieto-occipital sulcus. (c–d) Right occipital surface and its planar map. Bright color denotes gyrus regions with positive curvature, while dark color indicates sulcus regions with negative curvature. Calcarine sulcus, cuneus, and lingual gyri (red lines) are defined by principal curve tracking (Ratnanather et al., 2003).

Surface-based representation of functional response

Obtaining a surface-based representation of functional response requires a reduction of dimensionality, the assignment of the functional data in the 3D volume to locations on the cortical surface. We consider two steps that contribute to the mapping of a voxel in the functional statistical volume to a vertex on the cortical surface without considering potential misregistration of anatomical and functional volumes. The first step is to find the proper association between gray matter voxels and the cortical surface. Inappropriate association could, for instance, result in the assignment of the functional response of a voxel to the wrong bank of the calcarine sulcus. Several steps are necessary to find the proper association. We first label each voxel as GM, WM, or CSF and compute the shortest distance from each voxel to the surface. GM and CSF have positive outward distance, and WM has negative distance. A gray matter mask is created by taking into account all GM voxels less than 3 mm from the surface. This mask region is denoted as a set of voxels $P = \{i \,|\, d_i \leq 3\}$, where i is an index of the ith voxel and d_i is the shortest distance from this voxel to the surface. Assume a set V_j is the collection of all voxels in P closest to vertex v_j on the surface. The sets V_j, $j = 1, 2, \ldots, N_v$, where N_v is the number of vertices on the surface, represent the mapping of gray matter voxels to each vertex on the cortical surface. In the second step, we consider the contribution of distance d_i. Weighting data as a function of distance from the surface can reduce the impact of those voxels in the pial region (where there are large draining veins) that are far from the surface and perhaps misclassified as gray matter (Warnking et al., 2002).

In summary, functional statistic r_j for vertex j on the surface is defined as

$$\bar{r}_j = \frac{\sum_{i \in V_j} e^{-\frac{d_i^2}{2\sigma^2}} r_i}{\sum_{i \in V_j} e^{-\frac{d_i^2}{2\sigma^2}}}, \quad (1)$$

where r_i denotes the functional t statistic at voxel i and σ is the standard deviation of the weight function.

Smooth functional maps on the cortical surface

Surface-based representations of functional responses as a series of t statistic maps residing on the cortical surface are quite noisy due to the noise inherent in fMRI and the highly convoluted nature of the cortical sheet. To increase the signal to noise ratio of functional maps, spatially smoothing functional activation on the cortical surface is needed and superior to smoothing in the fMRI volume because two adjacent voxels in the volume may not belong to the same anatomical structure (e.g., gyrus or sulcus). The intuition of our approach comes directly from the Fourier basis representation for smoothing functions on a regular grid. As demonstrated in Fig. 3a, a one-dimensional signal f can be represented as a linear combination of orthonormal basis functions (e.g., cosine functions,

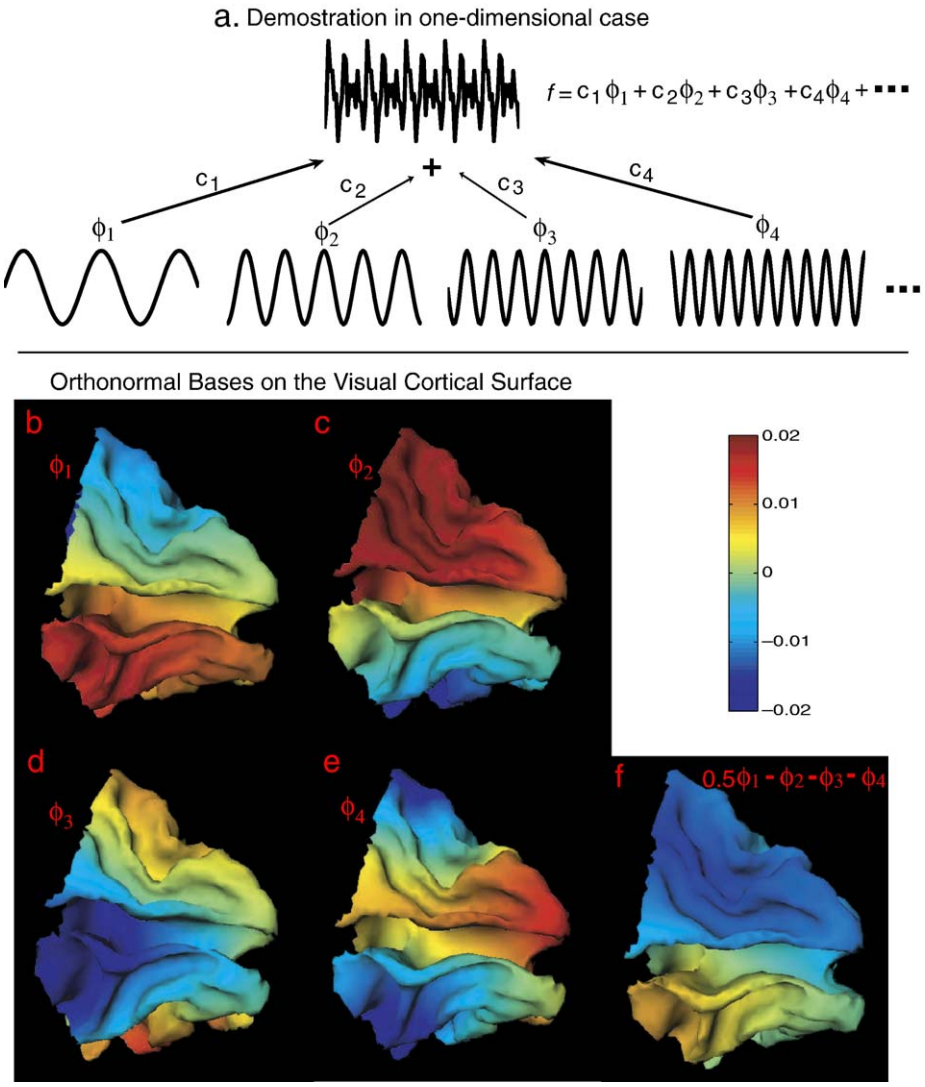

Fig. 3. (a) A signal in one dimension can be represented by a linear combination of orthonormal bases (e.g., cosine functions, ϕ_1, ϕ_2, ϕ_3, ϕ_4, ...). Panels b–e illustrate the first four orthonormal bases of the Laplace–Beltrami operator associated with the right visual cortical surface in Fig. 2c. Panel f gives an example of the function constructed from a linear combination of orthonormal basis functions shown on panels b–e.

Fourier bases). Therefore, the smoothed function f can be obtained by variety of stochastic signal processing methods using these orthonormal basis functions (e.g., $f = c_1\phi_1 + c_2\phi_2 + \ldots$ on Fig. 3a).

Finding orthonormal basis functions on the cortical surface, which incorporate the geometry of the highly curved cortex, is the key to allow classical stochastic signal processing on a regular grid to be performed on the cortical surface. The Laplace–Beltrami operator, the extension of the Euclidean Laplacian to an arbitrary Riemannian surface, has a positive definite property and allows us to compute a complete set of orthonormal bases. The Laplacian incorporates the intrinsic properties of the geometry of a curved surface in the sense that it takes the interior angles and areas of triangles into account, which are related to the curvature information on the discrete triangulated surface (Meyer et al., 2002). In Appendix A, we show the formulation of bases of the Laplace–Beltrami operator on the cortical surface and spline smoothing of functional maps via these bases, a generalization of the spline smoothing problem in a reproducing kernel Hilbert space from unit sphere to an arbitrary surface (Wahba, 1990).

Estimating the ridge of maximal activation via dynamic programming

We localize the functional response to each annular ring stimulus on the smoothed functional map and build the correspondence between annular rings in the visual field and their functional responses in the visual cortex via dynamic programming (DP). Because the blood oxygenation level dependent (BOLD) fMRI response is an indirect and blurry measurement of the neural response, it is difficult to localize and separate the functional responses to each individual ring. Additionally, the location of a ring's response cannot be characterized by the estimated midpoint of the activation boundaries because these boundaries are threshold dependent and may be asymmetrically distant from the true ridge of maximum activation due to cortical magnification. Here, we track the ridge of maximal activation directly because it is independent of threshold and thus more reliable. Such a ridge is defined as the path that has the minimal cost among candidate curves $\alpha(s, t)$ on the surface, where s and t

are the starting and ending points, respectively. The cost function has the form:

$$\int_{\alpha(s,t)} (r(\mathbf{x}) - R)^2 d\alpha, \tag{2}$$

where $r(\mathbf{x})$ is the functional statistic at the location $\mathbf{x}$ on the surface. We use the t statistic to characterize the functional response. R is assigned as the largest value of the t statistic on the surface.

DP is adapted to the above optimization problem on the triangulated surface (Khaneja et al., 1998). Define N_v and N_T as the number of vertices and triangles on the surface $\mathcal{M}$, respectively. Denote the index of each vertex on the surface as i, $i = 1, 2, \ldots, N_v$, and its coordinates in $\mathbb{R}^3$ as $\mathbf{x}_i$, and a triangle on the surface as T_j, $j = 1, 2, \ldots, N_T$. If the vertex i is one of three vertices within triangle T_j, then we say $i \in T_j$. Define the platelet $\mathcal{N}_i$ as the set of vertices for which there is an edge e_{ij} connecting it with vertex i, written as

$$\mathcal{N}_i = \{ j \,|\, e_{ij} \in \mathcal{M}, j = 1, 2, \ldots, N_v, j \neq i \}.$$

Define a path on the surface routed and terminated respectively in vertices s and t on the surface as

$$(s = j_1, j_2), \ldots, (j_{k-1}, j_k), \ldots, (j_{N-1}, t = j_N),$$

such that $j_k \in \mathcal{N}_{j_{k-1}}$ for $\forall k$. Define the set of paths with connecting vertices s and t on the surface $\mathcal{M}$ as $P(s, t)$, and (s, t) as a path that belongs to $P(s, t)$. Then the ridge of maximal activation is defined as the cost-minimizing path given by

$$\hat{\alpha}(s, t) = \mathrm{argmin}_{\alpha(s,t) \in P(s,t)} \mathcal{C}_\alpha(s, t), \tag{3}$$

where

$$\mathcal{C}_\alpha(s, t) = \sum_{k=1}^{N} \left(R - \frac{r_{j_k} + r_{j_{k+1}}}{2} \right)^2 ||\mathbf{x}_{j_k} - \mathbf{x}_{j_{k+1}}||. \tag{4}$$

Notice, when r is constant, α is the path between vertices s and f with the shortest geodesic length on the surface. In addition, if the t value is used, the ridge of minimal activation is defined in the same way by replacing R with the smallest t value.

Estimating linear cortical magnification

The linear cortical magnification factor quantifies the spatial sampling in area V1, which is expressed in terms of millimeters of cortex per degree of visual angle. As described in Section Estimating the ridge of maximal activation via dynamic programming, we associate a ridge of maximum activation with the center of each stimulus ring. We then choose one ridge as a reference and compute the geodesic distances (i.e., distance along the folded cortical surface) between the reference ridge and each of the other ridges. The geodesic distance is determined as follows. Define the reference ridge as ℓ_0, and a point on ℓ_0 as p_i, $i = 1, 2, \ldots, N_0$. Similarly, define the other ridge as ℓ_1, and a point on ℓ_1 as q_j, $j = 1, 2, \ldots, N_1$. If d_{0i} and d_{1j} are the shortest distances of a point p_i on ℓ_0 to ℓ_1 and a point q_j on ℓ_1 to ℓ_0, respectively, then the geodesic distance d between ℓ_0 and $\ell_1$is defined as

$$d = \frac{\bar{d}_0 + \bar{d}_1}{2}, \tag{5}$$

where

$$\bar{d}_0 = \frac{1}{N_0} \sum_{i=1}^{N_0} d_{0i} \text{ and } \bar{d} = \frac{1}{N_1} \sum_{j=1}^{N_1} d_{1j}. \tag{6}$$

d_{0i} and d_{1j} are computed using the Dijkstra algorithm (Dijkstra, 1959), which finds the shortest path between points on the cortical surface.

We plot the eccentricity θ corresponding to the peak of each ridge as a function of cortical distance d and fit the curve as the exponential function $\theta = e^{c(d + d_0)}$ (Engel et al., 1997). d_0 denotes the translation distance, which depends on which ridge is chosen as the reference line. We are only interested in parameter c since it is a scale factor inversely proportional to the linear cortical magnification factor, $M(\theta) = (dd/d\theta) = (1/c)\theta^{-1}$ mm/degree, which expresses the change in the cortical distance produced by a unit degree of the visual field at any given eccentricity. This is derived as follows:

$$d = \frac{1}{c} \ln(\theta) - d_0,$$

$$\frac{dd}{d\theta} = \frac{1}{c} \theta^{-1}.$$

The parameters are estimated using the least square method.

Results

We studied the retinotopic map in a population of five young adults (four males and one female) with normal vision and no known neurological impairments.

Smoothed functional maps

There are no closed mathematical expressions for generating a complete orthonormal basis for an arbitrary surface. Fig. 3 illustrates the numerical solutions to basis functions on the visual cortical surface. Panels b–e demonstrate the first four basis functions (ϕ_1, ϕ_2, ϕ_3, ϕ_4), which are functionally equivalent to the ones (ϕ_1, ϕ_2, ϕ_3, ϕ_4) shown on panel a except the ones on panel (a) are for the one-dimensional case. Red denotes positive value regions, and blue denotes negative value regions. As one goes to higher orders of the basis functions, the alternating red/blue pattern varies rapidly, implying the inclusion of high frequency components; this is similar to what we demonstrated in the one-dimensional case on panel a. Panel f gives an example of the function constructed from a linear combination of orthonormal basis functions (ϕ_1, ϕ_2, ϕ_3, ϕ_4) shown on panels b–e on the visual cortical surface.

Fig. 4 compares unsmoothed and smoothed functional maps. The first row shows functional maps of the horizontal meridian on the right visual cortical surface (see its 3D surface in Fig. 2c). Panel a illustrates the unsmoothed functional map on the surface. For purposes of visualization, panels b and c show the unsmoothed and smoothed functional maps, respectively, on the plane. The second row shows the functional map of one ring. As in the top row, panels d–f show the unsmoothed map on the surface and on the plane and the smoothed map on the plane.

Ridge tracking

In this section, we present the results of ridge tracking, quantify the potential effects of starting and ending point selection, and illustrate how the ridge passes through the activated region. The ridge tracking results are visualized on the 2D plane, but all calculations are performed on the folded cortical surface.

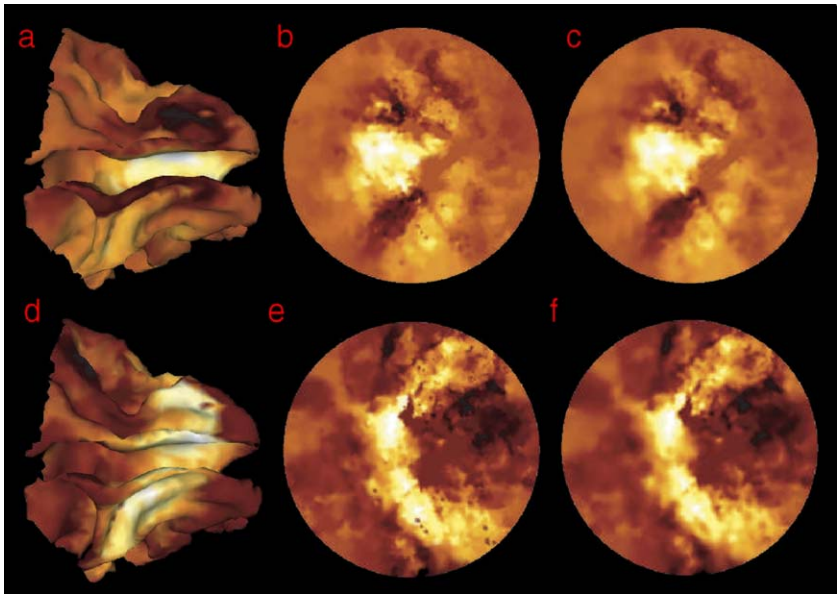

Fig. 4. Functional statistical maps on the right visual surface (see Fig. 2c for the 3D surface and Fig. 2d for the planar map). Bright color represents the high t value region, while dark color denotes the low t value region. The functional responses to the horizontal and vertical meridia are shown on the first row, and the functional response to one ring is shown on the second row. Panels a and d show unsmoothed functional responses on the cortical surface. Panels b and e illustrate the unsmoothed functional responses on the planar map. Panels c and f show smoothed functional maps.

We first delimit the V1 boundary by defining the ventral and dorsal vertical meridian ridges (evoked by stimulating the upper and lower visual field meridia, respectively) and marking the center of V1 using the horizontal meridian response on the surface. Figs. 5a–c show the functional maps for each of these meridian wedges. Negative t values denote the vertical meridian wedges (dark color) and positive t values are associated with the horizontal meridian wedge in the contralateral visual hemifield (bright color). For the ridges corresponding to the vertical meridian wedges, we manually initialize the starting and ending points, after which the path is automatically tracked via dynamic programming as defined in Eq. (4) where R is the minimum value on the surface. The ridge for the horizontal meridian wedge is found in a similar way, except R is the maximum value on the surface in Eq. (4) and the starting and ending points are chosen halfway between the two vertical meridian ridges. The ventral and dorsal vertical meridian ridges on the surface define the borders between area V1 and areas V2v and V2d, respectively. The horizontal meridian ridge separates the V1 regions associated with the upper and lower quadrants within the visual hemifield represented in each hemisphere of the brain.

To track the ridge of maximum activation evoked by each ring, a starting point and ending point are selected that fall on the ventral and dorsal boundaries of V1, respectively. Panel d shows the center of each ring in the visual field using different colors; these eccentricities are marked above each panel from e–k. For instance, the inner and outer boundaries of the first ring are 1.62° and 3.24° of visual angle, respectively, so the center of this ring has an eccentricity of 2.43°. Panels e–k illustrate the ridge of maximum activation for each ring on the surface using the same color scheme as in panel d. As visual field eccentricity increases across stimulus rings, the corresponding ridges move from posterior to anterior visual cortex, as shown on panel (l). The background in panel (m) gives the anatomical structure of this surface: bright color denotes gyrus (positive curvature) regions while dark color represents sulcus (negative curvature) regions; red lines are defined as the principal curves of the cuneus gyrus, calcarine sulcus, and lingual gyrus (Ratnanather et al., 2003) from top to bottom.

Convergence

The above dynamic programming tracking procedure involves the manual selection of the starting and ending points for each ring. Fig. 6 illustrates how the solution is affected by the selected initial points. Panels a–b show the functional map (also shown in Fig. 5e) on the surface and plane, respectively. Red, blue, and green paths are tracks found using different initial points separated by approximately 2 mm on the cortical surface. These three paths converge after just two or three tracking nodes, suggesting high stability of the algorithm.

Definiteness

Fig. 7 illustrates the distribution of functional t statistics on 10 curves (colored blue in panel a) perpendicular to the ridge representing the innermost ring and shows the location of the tracking ridge on the activation region. These curves are indexed as 1, 2, . . . , 10 from the top to the bottom. Every point on each of the curves is also indexed as 1, 2, . . . M. The functional t statistic as a function of these indices is illustrated on panel b, where x, y, and z axes are indices of curves, points on the curves, and functional t statistic, respectively. Red *s denote the locations where the ridge passes through each curve. The ridge crosses each curve approximately at the point where the maximum functional t statistic occurs.

Linear cortical magnification

Fig. 8 shows retinotopic eccentricity maps of the primary visual cortex for the left and right hemispheres in all five subjects. The ridges of maximum activation for each ring on

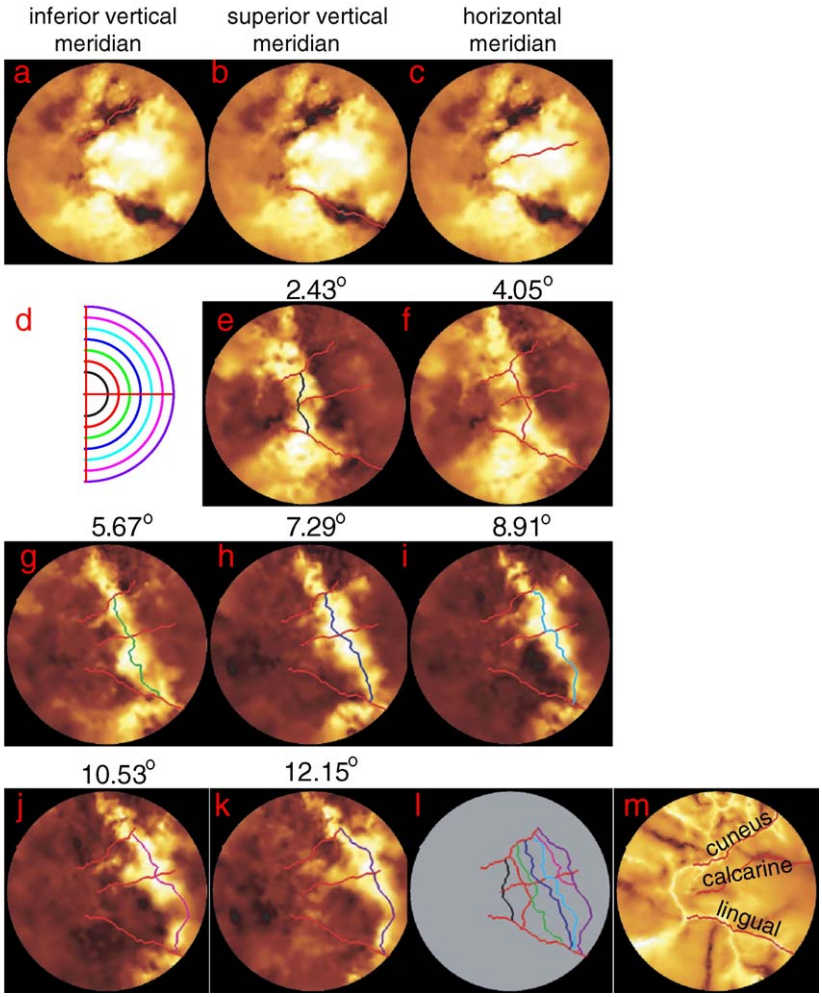

Fig. 5. Ridge tracking on the left occipital cortex. Panels a–c show vertical and horizontal meridia on the functional map. Ridges of maximum activation are tracked by dynamic programming and are denoted by red lines. Panel d illustrates the left visual field with seven equal-width rings. Each semicircle represents the center of the ring indicated by different colors to be associated with each ridge tracked on a functional map shown on panels e–k. The functional response to each individual ring (ring centers from 2.43° to 12.15°) is shown on panels e–k, respectively. The lines on these panels indicate the locations of the ridges of maximum activation associated with the centers of the ring stimuli. The tops of panels give the eccentricities of the centers of the ring stimuli in the visual field. Brightness indicates the t value. Panel l gives the overall view of seven ridges on the 2D plane and panel m illustrates the anatomical structure with the curvature information as the background. The anatomical landmarks of the visual cortex are defined by the principal curve tracking algorithm (Ratnanather et al., 2003) and are shown by the red lines on panel m.

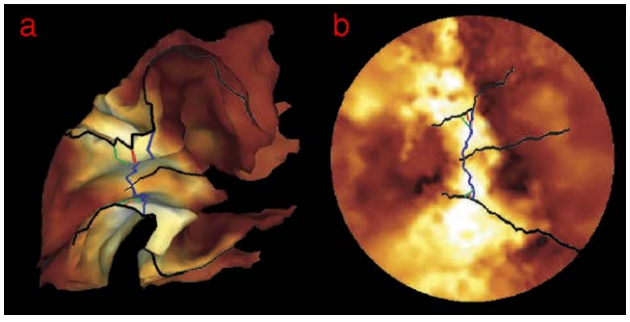

Fig. 6. Convergence analysis of the sensitivity of ridge tracking to variation of starting and ending points. Panels a–b show the functional map on the surface and plane, respectively. Three paths in red, blue, and green are tracked by giving different starting and ending points to find the ridge of maximal activation. The ridges tracked between each set of starting and ending points converge within 2–3 tracking nodes.

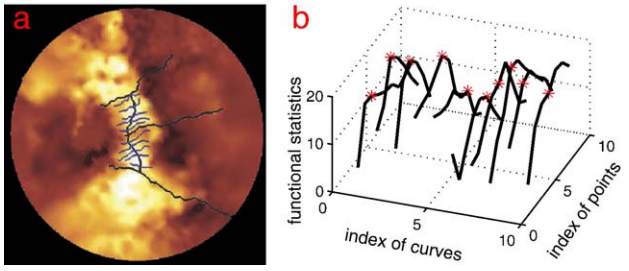

Fig. 7. Definiteness of ridge tracking. Panel a gives the functional map to the first ring, which is also shown in Fig. 6b. The 10 blue curves are approximately equally spaced and perpendicular to the ridge of maximal activation from the first ring. They are indexed as 1, 2, . . . , 10 from the top to the bottom. Panel b demonstrates the functional statistic of the ridge through the activation region. The x-axis indexes the blue curves; the y-axis indexes the points on each blue curve; the z-axis shows the functional statistic for each point of the curve. Red *s represent the point where the ridge passes through each of the blue curves.

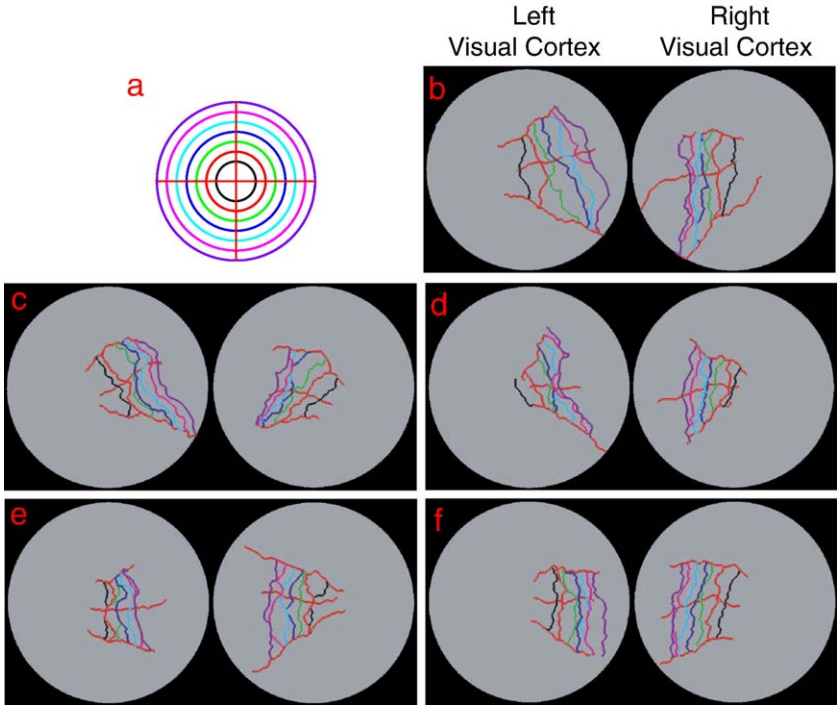

Fig. 8. Retinotopic eccentricity maps. Panel a gives the schematic denoting the center of the seven rings, each colored differently in the visual space. The remaining panels illustrate the ridges of responses on the left and right visual cortical surfaces for each subject.

panels (b)–(f) are colored as in the visual field representation on panel (a). Figs. 5m and 2d show anatomical structures of the left and right visual cortices as references. The left visual cortex is activated by stimuli in the right visual field, while the right visual cortex is activated by stimuli in the left visual field. As ring radii increase, the associated functional responses move from posterior to anterior visual cortex. Some of the ridges touch due to overlapping functional responses, but no ridges cross. Notice that the ridges appear jagged on the flattened representation of the cortical surface because the flattening procedure used in this paper preserves angles, but not geodesic distance. Therefore, the abutting ridges on the flattened map do not indicate that the geodesic distance between them is small on the 3D cortical surface.

Fig. 9 shows the visual field eccentricity as a function of the geodesic distance from the reference ridge (center eccentricity, 2.43°) to each of the other six ridges corresponding to stimulus rings with center eccentricities up to 12.15° in 1.62° increments. The geodesic distances are measured from each ridge to the reference ridge on the GM/WM 3D cortical surface using the ridge over the full hemifield (ventral and dorsal V1). Each circle or diamond in Fig. 9, colored differently to distinguish between subjects, represents one distance measurement on the left or right visual cortex for the full visual hemifield space. The mean across subjects is shown by the black line. The red curve is the exponential function $\theta = e^{0.0742(d + 13.71)}$, which best fits (least square method) the data. The linear cortical magnification is then simply described as $M(\theta) = (1/0.0742)\theta^{-1} = 13.48\theta^{-1}$.The last column of Table 2 lists the best fits for measurements from each left and right full hemifields in all subjects. Fig. 9 and the last column of Table 2 indicate that there are individual differences in linear cortical magnification, and within-subject differences between hemispheres.

Multirun reliability

To test the multirun reliability of the linear cortical magnification estimates, we split the set of all ring runs into the odd- and even-numbered runs. Then, we repeated all fMRI analysis and ridge tracking analysis to estimate the linear cortical magnification factor for these two groups separately. Table 1 lists all estimates for the groups of odd and even runs as well as all runs. Fig. 10a shows that the scale factor c from the groups of odd and even runs is highly correlated with that in the group of all runs (correlation

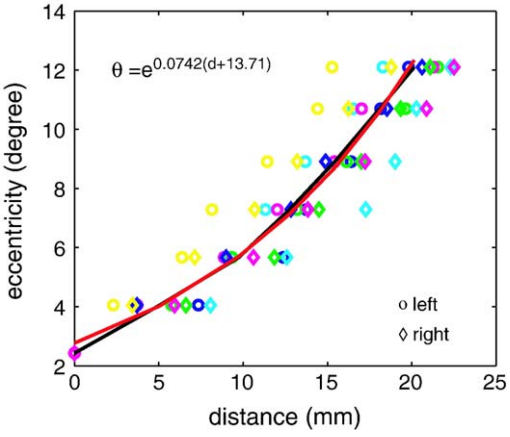

Fig. 9. Eccentricity as a function of the geodesic distance from reference (2.43°) ridge in V1 for the full visual hemifield in five normal subjects. Circles and diamonds denote each measurement on the left and right visual cortex, respectively, and are colored to distinguish each subject. The mean measurement curve among the five subjects is represented by black lines; the red line is the fitted curve using the exponential function $\theta = e^{c(d + d_0)}$.

Table 1
Multirun reliability in linear cortical magnification estimation

	Odd runs			Even runs			All runs		
	c	d_0	$M(\theta)$	c	d_0	$M(\theta)$	c	d_0	$M(\theta)$
Subject 1									
Left	0.083	12.03	$12.05\theta^{-1}$	0.087	11.13	$11.49\theta^{-1}$	0.080	13.18	$12.50\theta^{-1}$
Right	0.075	10.73	$13.33\theta^{-1}$	0.070	13.21	$14.29\theta^{-1}$	0.078	9.31	$12.82\theta^{-1}$
Subject 2									
Left	0.112	9.01	$8.93\theta^{-1}$	0.107	10.25	$9.35\theta^{-1}$	0.089	8.24	$11.24\theta^{-1}$
Right	0.073	13.70	$14.08\theta^{-1}$	0.068	15.13	$14.71\theta^{-1}$	0.068	16.34	$14.71\theta^{-1}$
Subject 3									
Left	0.073	15.07	$13.70\theta^{-1}$	0.073	14.62	$13.70\theta^{-1}$	0.067	15.90	$14.93\theta^{-1}$
Right	0.073	10.99	$13.70\theta^{-1}$	0.074	10.33	$13.51\theta^{-1}$	0.078	11.04	$12.82\theta^{-1}$
Subject 4									
Left	0.077	15.70	$12.99\theta^{-1}$	0.078	16.22	$12.82\theta^{-1}$	0.085	13.93	$11.76\theta^{-1}$
Right	0.076	15.90	$13.16\theta^{-1}$	0.073	16.53	$13.70\theta^{-1}$	0.072	16.36	$13.89\theta^{-1}$
Subject 5									
Left	0.064	18.30	$15.63\theta^{-1}$	0.064	18.17	$15.63\theta^{-1}$	0.065	18.08	$15.38\theta^{-1}$
Right	0.067	16.07	$14.93\theta^{-1}$	0.066	15.54	$15.15\theta^{-1}$	0.065	16.00	$15.38\theta^{-1}$

Note. The eccentricity is described as an exponential function of the geodesic distance, $\theta = e^{c(d + d_0)}$, where c is the scale factor and d_0 denotes the translation distance relative to the reference ridge. The linear cortical magnification factor, $M(\theta)$, is described as a function of eccentricity, $M(\theta) = (1/c)\theta^{-1}$.

coefficient: 0.7933; $P < 0.001$). Similarly, panel (c) illustrates that the correlation coefficient of the scale factor c between odd and even runs is high (correlation coefficient: 0.9725; $P < 0.001$). In addition, correlation coefficients of the scale factor c in odd vs. all and even vs. all are 0.7788 ($P = 0.008$) and 0.8110 ($P = 0.004$), respectively. Overall, these correlations show that the variability of our linear cortical magnification estimates is not significantly large across fMRI runs.

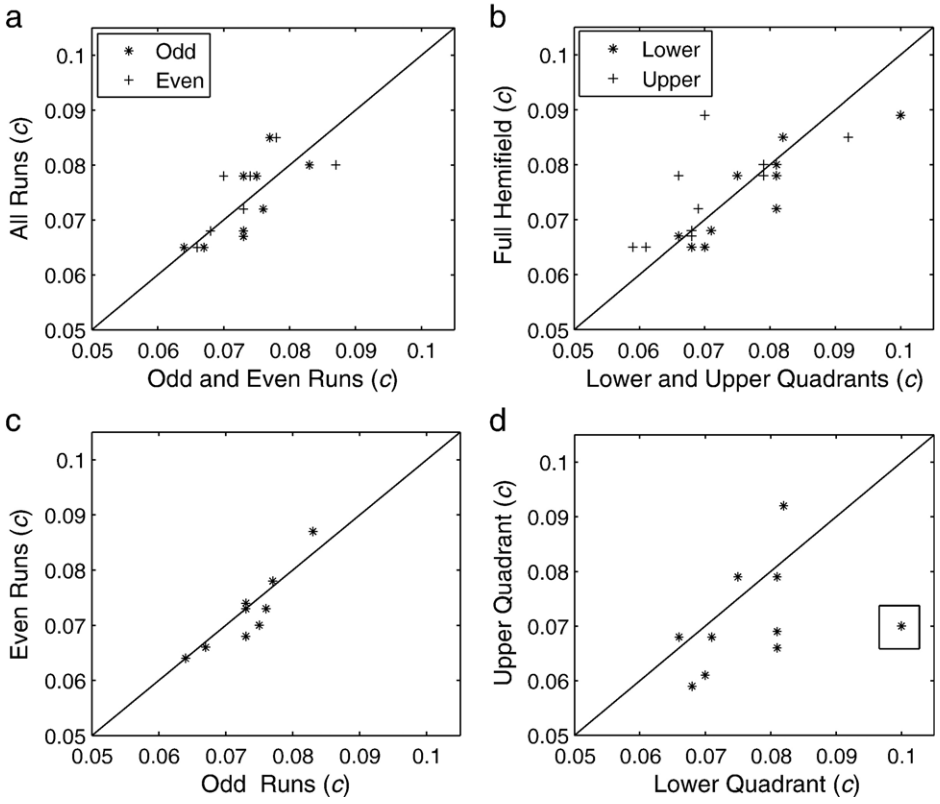

Fig. 10. Reliability of the estimates of linear cortical magnification factor. (a) Correlation plot of the scale factor c between half of the runs (odd and even) and all runs. The correlation coefficient is 0.7933 and $P < 0.001$. (b) Correlation plot of the scale factor c between quadrants (lower and upper) and the full hemifield. The correlation coefficient is 0.7429 and $P < 0.001$. (c) Correlation plot of the scale factor c between the odd and even sets of runs. The correlation coefficient is 0.9725 and $P < 0.001$. (d) Correlation plot of the scale factor c between lower and upper quadrants. The correlation coefficient is 0.3409 and $P = 0.3351$. However, if one outlier (in the rectangular frame) is removed, the correlation becomes 0.6140 ($P = 0.078$). Each data point represents one measurement from left or right hemisphere of five subjects.

Spatial reliability

To test the stability of the linear cortical magnification estimates, we divide each visual hemifield into two quadrants (left upper and lower, right upper and lower; shown on Fig. 8b). For each quadrant, ridges corresponding to each ring are tracked between the horizontal meridian and either the dorsal or ventral V1 boundary (corresponding to the lower or upper vertical meridian, respectively) and the linear cortical magnification factor is measured. Table 2 lists all estimates for each quadrant and full hemifield. Fig. 10b shows that the scale factor c from lower and upper quadrants is highly correlated with that in the full hemifield (correlation coefficient: 0.7429, $P < 0.001$). In addition, correlation coefficients of the scale factor c in lower vs. full hemifield, upper vs. full hemifield, and lower vs. upper quadrants are 0.8837 ($P < 0.001$), 0.6849 ($P = 0.0289$), and 0.3409 ($P = 0.3351$), respectively. The low correlation between lower and upper quadrants is due to one outlier (shown in the rectangular frame on Fig. 10d), subject 2 left lower quadrant vs. left upper quadrant, listed in Table 2. If the outlier is excluded from the correlation calculation, the correlation coefficient between lower and upper quadrants increases from 0.3409 to 0.6140 ($P = 0.078$). Each data point in Fig. 8 represents one measurement from left or right hemisphere of five subjects. Overall, these correlations show that the linear cortical magnification estimate for one quadrant could be used to predict the linear cortical magnification for the other quadrant within the same hemifield.

Conclusion and discussion

This paper presents methods for retinotopic eccentricity mapping and linear cortical magnification estimation in human primary visual cortex using fMRI and dynamic programming methods. We studied retinotopic eccentricity maps of left and right visual cortices in five normal subjects. Primary visual cortex boundaries are defined by the vertical meridia; the horizontal meridian separates each visual hemifield into upper and lower quadrants. The ridge of maximum activation evoked by each ring was tracked via dynamic programming optimization over all possible paths on the cortical surface. The sequentially additive costs for the dynamic programming were constructed from the maximal (or minimal) t statistic superimposed on the local coordinate system of the cortical surface. The geodesic distances between the ridges were calculated via the Dijkstra algorithm. Finally, the visual field eccentricity was modeled as an exponential function of geodesic distance on the cortical surface, $\theta = e^{c(d + d_0)}$, and then the linear cortical magnification factor, $M(\theta)$, was simply described as $M(\theta) = (1/c)\theta^{-1}$.

In this paper, our efforts focused on assigning the functional volume data to the cortical surface, smoothing the functional statistical map directly on the cortical surface, and localizing functional responses on the cortical surface via dynamic programming. Our approach to assigning functional volume data to the cortical surface considers how to correctly associate GM voxels with cortical surface vertices to avoid assigning activations to an incorrect anatomical location. We augmented the standard MRI image indexed over the regular lattice of voxels $I(x_k)$, $k = 1, 2, \ldots$, with the secondary local normal distance coordinates, labeling each voxel x_k with its distance d to the GM/WM surface as a basic data structure (Barta et al., 2005). Such a data structure describes the laminar structure of the cortex in the sense that tissue properties change as a function of the normal distance from the local coordinates of the cortical surface. WM has negative distance, while GM and CSF have positive distance. CSF, however, has greater distance than GM. Such intensity and distance information gives a rough estimate of the local cortical thickness, which determines the association of the functional activation in GM with the cortical surface. Voxels in a deep sulcus, where there is no evidence of CSF due to partial-volume effects and the resolution of MRI, are equally assigned to the two banks of the sulcus. This assignment assumes that the two banks of the sulcus are of equal thickness. Even if this assumption is unwarranted, the distance weighting expressed in Eq. (1) should reduce the effect of assigning middle voxels (usually with great distance) to the wrong bank.

The orthonormal basis functions derived from the Laplace–Beltrami operator for any arbitrary curved surface play the same role as Fourier bases in smoothing data on a regular grid. The smoothing procedure introduced here is an approach for solving spline smoothing problems on the surface in a reproducing kernel Hilbert space of real-valued functions that satisfy continuity and the first-order differentiability. The Laplace–Beltrami operator is expressed as a weighted averaging operator where the weights are expressed in terms of the interior angles and areas of triangles, and

Table 2
Linear cortical magnification estimation in the lower quadrant, upper quadrant, and full hemifield

	Lower quadrant			Upper quadrant			Full hemifield		
	c	d_0	$M(\theta)$	c	d_0	$M(\theta)$	c	d_0	$M(\theta)$
Subject 1									
Left	0.081	12.08	$12.35\theta^{-1}$	0.079	14.30	$12.66\theta^{-1}$	0.080	13.18	$12.50\theta^{-1}$
Right	0.081	8.14	$12.35\theta^{-1}$	0.066	14.53	$15.15\theta^{-1}$	0.078	9.31	$12.82\theta^{-1}$
Subject 2									
Left	0.100	8.17	$10.00\theta^{-1}$	0.070	13.65	$14.29\theta^{-1}$	0.089	8.24	$11.24\theta^{-1}$
Right	0.071	15.10	$14.08\theta^{-1}$	0.068	15.63	$14.71\theta^{-1}$	0.068	16.34	$14.71\theta^{-1}$
Subject 3									
Left	0.066	18.55	$15.15\theta^{-1}$	0.068	13.11	$14.71\theta^{-1}$	0.067	15.90	$14.93\theta^{-1}$
Right	0.075	9.39	$13.33\theta^{-1}$	0.079	11.74	$12.66\theta^{-1}$	0.078	11.04	$12.82\theta^{-1}$
Subject 4									
Left	0.082	14.59	$12.20\theta^{-1}$	0.092	12.30	$10.87\theta^{-1}$	0.085	13.93	$11.76\theta^{-1}$
Right	0.081	11.33	$12.35\theta^{-1}$	0.069	19.01	$14.49\theta^{-1}$	0.072	16.36	$13.89\theta^{-1}$
Subject 5									
Left	0.070	16.63	$14.29\theta^{-1}$	0.061	19.80	$16.39\theta^{-1}$	0.065	18.08	$15.38\theta^{-1}$
Right	0.068	14.56	$14.71\theta^{-1}$	0.059	18.77	$16.95\theta^{-1}$	0.065	16.00	$15.38\theta^{-1}$

the connectivity of the mesh, which correspond to the intrinsic geometry of the cortical surface. The first derivative of the functional t statistic on the cortical surface controls the smoothness of the functional map. The use of such a procedure reduces the ridge tracking error and makes the ridge tracking more stable (see Fig. 7b). This procedure helps to accurately identify the activated region since an isolated activation will be suppressed by its inactive neighboring regions.

Our procedure defines the ridge of maximum functional activation automatically, except for the manual definition of initial starting and ending points that are easily chosen on the functional statistical maps without any experience and do not affect the estimation result (see Fig. 6). Our method avoids the necessity of manually drawing a reference line on the functional statistical map (Engel et al., 1997), which could induce error in estimating the linear cortical magnification. Moreover, template fitting approaches (Duncan and Boynton, 2003; Dougherty et al., 2003) are sensitive to the initial position of the template and need to involve a human expert initializing the template position and size in order to avoid yielding incorrect "local" solutions. In addition to that, the assumption that the mapping from the visual space to the two-dimensional flattened visual cortex is conformal has been made in the template fitting procedure in Duncan and Boynton (2003), which is strict and not necessarily true for each individual. Moreover, the distortion in the cortical flattening procedure is incorporated into the distance calculation, which introduces errors in estimating the linear cortical magnification. Our approach is model free and the peak of the activity is defined in a completely data-driven fashion. The two-dimensional flattened map is not needed to define the peak of the activity and the geodesic distance is directly computed on the folded cortical surface in our approach.

Fig. 11 shows estimates of the linear cortical magnification factor, $M(\theta)$, from the present and previous studies (Horton and Hoyt, 1991; Sereno et al., 1995; Engel et al., 1997; Duncan and Boynton, 2003). The black curve shows that the linear cortical magnification factor is inversely proportional to the eccentricity ($M(\theta) = 13.48\theta^{-1}$) in this study. Green, blue, red, and cyan curves give the linear magnification factor measurement as a function of the eccentricity in the previous studies. Sereno et al. (1995) gave $M(\theta) = 20.05\,(\theta + 0.08)^{-1.26}$; Engel et al. found $\theta = e^{0.063(d + 36.54)}$, which implies $M(\theta) = 15.87\theta^{-1}$; Duncan and Boynton (2003) showed $M(\theta) = 9.81\theta^{0.83}$. Horton and Hoyt (1991) gave $M(\theta) = 17.3(\theta + 0.75)^{-1}$, which is the result of the magnification for the macaque striate cortex, $M(\theta) = 12.0(\theta + 0.75)^{-1}$, adapted to the dimensions of the human striate cortex by an area factor (square root of the ratio of the human striate cortex average area 2500 mm^2 to the macaque striate cortex mean area 1200 mm^2). The curves indicate that the various measurements of $M(\theta)$ are in close agreement. Our magnification estimate near the fovea (up to around 3 degrees) is coincident to that of Horton and Hoyt (1991). However, according to Sereno et al. (1995) and Engel et al. (1997), $M(\theta)$ is somewhat larger near the fovea than estimated in the present study and by Horton and Hoyt (1991). The estimates may differ because of potential stimulus wrap-around with the expanding-ring stimuli used by Sereno et al. (1995) and Engel et al. (1997). Moreover, Sereno's estimate of $M(\theta)$ might be low in the periphery for the same reason. Duncan and Boynton (2003) measured the distance on a flattened map of the cortical surface, which does not preserve geodesic distances and may result in smaller estimate of $M(\theta)$ near the fovea than the other studies. Such distance distortion is likely to have a smaller effect on $M(\theta)$ in the periphery than in the fovea because of the relatively small amount of visual cortex representing the periphery.

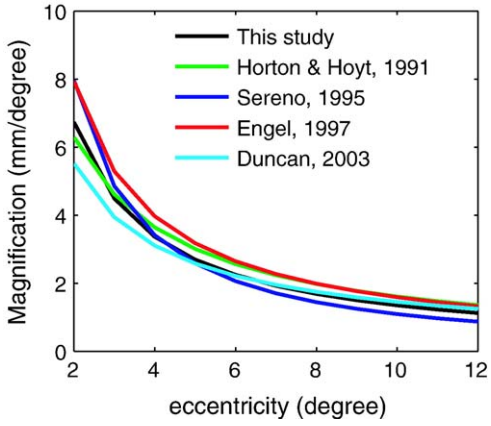

Fig. 11. Comparison of the linear cortical magnification estimates among the present and previous studies.

We validated the multirun and spatial reliability of our linear cortical magnification estimates by limiting the data to half runs or to quadrants, performing the estimation on these limited data sets, and then comparing these estimates to the estimates from the full data set. The multirun reliability study shows that there is no significant variability of the estimates across arbitrary chosen sets of fMRI runs. In addition, the results of our spatial reliability study show that cortical magnification is quite similar in the dorsal and ventral compartments of V1 within each hemisphere. The symmetry of cortical magnification across quadrants within a hemifield, together with the stability of the linear cortical magnification estimates, suggests that it may be possible to predict the linear cortical magnification factor in regions of cortex where retinotopic mapping is not possible due to loss of afferent input (e.g., local retinal damage), which could in turn be used to measure cortical plasticity following partial loss of visual input.

Acknowledgments

The work reported here was supported by NIH grants: 1 P41 RR15241, 1 R01 EB00975, 1 P20 MH621130, and 1 R01 DA13165. The authors thank Dr. Xiao Han of Massachusetts General Hospital for the topology-correction method and the connectivity-consistent isosurface algorithm. The authors also thank Dr. Ken Stephenson of University of Tennessee for providing CirclePack software (http://www.math.utk.edu/kens) to create the hyperbolic maps.

Appendix A. Bases of the Laplace–Beltrami operator and spline interpolation

Consider a smooth orientable surface $\mathcal{M}$ embedded into $\mathbb{R}^3$. We choose to describe $\mathcal{M}$ by means of a parameterization $\mathbf{x} : \mathcal{D} \subset \mathbb{R}^2 \mapsto \mathbb{R}^3 : \mathbf{x}(\mathbf{u}) = \begin{bmatrix} x_1(\mathbf{u}) \\ x_2(\mathbf{u}) \\ x_3(\mathbf{u}) \end{bmatrix}$, where $\mathbf{u} = (u_1, u_2) \in \mathcal{D}$. The parameters u_1 and u_2 play the role of local coordinates on the surface. The problem is to seek the complete orthonormal basis (ϕ, λ) of the Laplace–

Beltrami operator with Neumann boundary conditions on the surface posed as:

$$\Delta\phi(\mathbf{u}) + \lambda\phi(\mathbf{u}) = 0 \text{ in } \mathcal{M},$$

$$\int_{\mathcal{M}} |\phi(\mathbf{u})|^2 d\mathcal{M} = 1,$$

$$< \nabla\phi(\mathbf{u}), \mathbf{n} > |_{\partial\mathcal{M}} = 0, \tag{7}$$

where Δ is the Laplace–Beltrami operator; $\partial\mathcal{M}$ denotes the boundary of $\mathcal{M}$; $\mathbf{n}$ is the normal vector on the boundary of $\mathcal{M}$. Eigen-elements of the Laplace–Beltrami operator are denoted as $(\phi(\mathbf{u}), \lambda)$.

Computing the basis is equivalent to solving the weak form of the eigenvalue problem:

$$\{\phi(\cdot), \lambda\} = \underset{\phi(\cdot),\lambda}{\operatorname{argmin}} E(\phi(\cdot), \lambda), \tag{8}$$

where

$$E(\phi(\cdot), \lambda) = \int_{\mathcal{M}} ||\nabla\phi(\mathbf{u})||^2 d\mathcal{M} - \lambda \int_{\mathcal{M}} |\phi(\mathbf{u})|^2 d\mathcal{M}. \tag{9}$$

Given the complete orthonormal basis, the smoothed functional map $\mathbf{r}(\mathbf{u})$ can be obtained by spline smoothing in a reproducing kernel Hilbert space of real-valued functions that satisfy the continuity and first order differentiability conditions (Wahba, 1990) and minimize:

$$\hat{r}(\mathbf{u}) = \underset{r(\cdot)}{\operatorname{argmin}} \int_{\mathcal{M}} ||\nabla r||^2 d\mathcal{M} + \gamma \sum_{j=1}^{N_v} \left(r(v_j) - \bar{r}_j\right)^2, \tag{10}$$

$$r(\mathbf{u}) = \beta_0 + \sum_{k=1}^{N_v} \beta_k G(\mathbf{u}, \mathbf{u}_k), \tag{11}$$

where the Green's function

$$G(\mathbf{u}_1, \mathbf{u}_2) = \sum_{i=1}^{\infty} \frac{1}{\lambda_i} \phi_i(\mathbf{u}_1)\phi_i(\mathbf{u}_2). \tag{12}$$

$r(v_j)$ represents the estimated functional response at vertex v_j, and r_j is the 3D data associated with the 2D surface given in Eq. (1). The first term in Eq. (10) controls the smoothness via the Green's function and the second term gives the prior information of the data. Here, we assume the noise is Gaussian distributed with variance σ^2.

For implementation, we first seek the numerical solution to (ϕ, λ) in Eq. (9) by the finite element method (Qiu et al., 2005), denoted as $(\mathbf{\Phi}, \lambda)$, where is a $\mathbf{\Phi}$ vector with basis value at each of N_v vertices on the surface. The orthonormal basis $\mathbf{\Phi}$ is normalized with respect to triangle areas and interior angles and connectivity of the surface mesh. The Green's function in the discrete version is defined as $G = \sum_1^{N_v} \frac{1}{\lambda_i} \mathbf{\Phi}_i \mathbf{\Phi}_i^t$, a $N_v \times N_v$ matrix, where ^{t} denotes matrix transpose. Assume that $\hat{\mathbf{r}}$ and $\bar{\mathbf{r}}$ are vectors with N_v entries of smoothed and unsmoothed functional response, respectively. All coefficients β_k are estimated by the least square method.

References

Andrade, A., Kherif, F., Mangin, J.F., Worsley, K.J., Paradis, A.L., Simon, O., Dehaene, S., Bihan, D.L., Poline, J.B., 2001. Detection of fMRI activation using cortical surface mapping. Hum. Brain Mapp. 12, 79–93.

Angenent, S., Haker, S., Tannenbaum, A., Kikinis, R., 1999. On the Laplace–Beltrami operator and brain surface flattening. IEEE Trans. Med. Imag. 18, 700–711.

Baker, C.I., Peli, E., Knouf, N., Kanwisher, N.G., 2005. Reorganization of visual processing in macular degeneration. J. Neurosci. 25, 614–618.

Barta, P., Miller, M.I., Qiu, A., 2005. A stochastic model for studying the laminar structure of cortex from MRI. IEEE Trans. Med. Imag. 24, 728–743.

Baseler, H.A., Morland, A.B., Wandell, B.A., 1999. Topographic organization of human visual areas in the absence of input from primary cortex. J. Neurosci. 19, 2619–2627.

Collins, C., Stephenson, K., 2003a. A circle packing algorithm. Comput. Geom. 25, 21–34.

Collins, C.R., Stephenson, K., 2003b. A circle packing algorithm. Comput. Geom. Theory Appl. 25, 233–256.

Dale, A.M., Sereno, M.I., 1993. Improved localization of cortical activity by combining EEG and MEG with MRI cortical surface reconstruction: a linear approach. J. Cogn. Neurosci. 5, 162–176.

Dale, A.M., Fischl, B., Sereno, M.I., 1999. Cortical surface-based analysis: I. Segmentation and surface reconstruction. NeuroImage 9, 179–194.

Daniel, P.M., Whitteridge, D., 1961. The representation of the visual field on the cerebral cortex in monkeys. J. Physiol. 159, 203–221.

DeYoe, E.A., Carmandagger, G.J., BandettiniDagger, P., Glickman, S., Wieser, J., Cox, R., Miller, D., Neitz, J., 1996. Mapping striate and extrastriate visual areas in human cerebral cortex. Proc. Natl. Acad. Sci. 93, 2382–2386.

Dijkstra, E.W., 1959. A note on two problems in connexion with graphs. Numer. Math. 1, 269–271.

Dougherty, R.F., Koch, V.M., Brewer, A.A., Fischer, B., Modersitzki, J., Wandell, B.A., 2003. Visual field representations and locations of visual areas V1/2/3 in human visual cortex. J. Vis. 3, 586–598.

Duncan, R.O., Boynton, G.M., 2003. Cortical magnification within human primary visual cortex correlates with acuity thresholds. Neuron 38, 659–671.

Engel, S.A., Rumelhart, D.E., Wandell, B.A., Lee, A.T., Glover, G.H., Chichilnisky, E.J., Shadlen, M.N., 1994. fMRI of human visual cortex. Nature 369, 525.

Engel, S.A., Glover, G.H., Wandell, B.A., 1997. Retinotopic organization in human visual cortex and the spatial precision of functional MRI. Cereb. Cortex 7, 181–192.

Fischl, B., Sereno, M.I., Dale, A.M., 1999a. Cortical surface-based analysis: II. inflation, flattening, and a surface-based coordinate system. NeuroImage 9, 195–207.

Fischl, B., Sereno, M.I., Tootell, R.B.H., Dale, A.M., 1999b. High-resolution inter-subject averaging and a surface-based coordinate system. Hum. Brain Mapp. 8, 272–284.

Fischl, B., Liu, A., Dale, A.M., 2001. Automated manifold surgery: constructing geometrically accurate and topologically correct models of the human cerebral cortex. IEEE Trans. Med. Imag. 20, 70–80.

Fischl, B., Salat, D.H., Busa, E., Albert, M., Dieterich, M., Haselgrove, C., van der Kouwe, A., Killiany, R., Kennedy, D., Klaveness, S., Montillo, A., Makris, N., Rosen, B., Dale, A.M., 2002. Whole brain segmentation: automated labeling of neuroanatomical structures in the human brain. Neuron 33, 341–355.

Friston, K.J., Jezzard, P., Turner, R., 1994. Analysis of functional MRI time-series. Hum. Brain Mapp. 1, C153–C171.

Han, X., Xu, C., Tosun, D., Prince, J.L., 2001. Cortical surface reconstruction using a topology preserving geometric deformable model. Workshop on Mathematical Methods in Biomedical Image Analysis, Kauai Hawaii, pp. 213–220.

Han, X., Xu, C., Braga-Neto, U., Prince, J., 2002. Topology correction in brain cortex segmentation using a multiscale, graph-based algorithm. IEEE Trans. Med. Imag. 21, 109–121.

Harris, G., Andreasen, N.C., Cizadlo, T., Bailey, J.M., Bockholt, H.J., Magnotta, V.A., Arndt, S., 1999. Improving tissue classification in MRI: a three-dimensional multi spectral discriminant analysis method with automated training class selection. J. Comput. Assist. Tomogr. 23, 144–154.

Holmes, G., 1918. Disturbances of vision by cerebral lesions. Br. J. Ophthalmol. 2, C353–C384.

Horton, J.C., Hoyt, W.F., 1991. The representation of the visual field in human striate cortex. a revision of the classic Holmes map. Arch. Ophthalmol. 109, 816–824.

Hurdal, M.K., Bowers, P.L., Stephenson, K., Sumners, D.L., Rehm, K., Schaper, K., Rottenberg, D.A., 1999. Quasi-conformally at mapping the human cerebellum. In: Taylor, C., Colchester, A. (Eds.), Lecture Notes in Computer Science. Springer-Verlag, Berlin, pp. 279–286.

Inouye, T., 1909. Visual Disturbances following Gun shot Wounds of the Cortical Visual Area (translated by M. Glickestein and M. Fahle). Oxford Univ. Press, Oxford 2000. (Suppl. 1-101).

Joshi, M., Cui, J., Doolittle, K., Joshi, S., Van Essen, D., Wang, L., Miller, M.I., 1999. Brain segmentation and the generation of cortical surfaces. NeuroImage 9, 461–476.

Kapur, T., Grimson, W.E.L., Wells, W.M. III, Kikinis, R., 1996. Segmentation of brain tissue from magnetic resonance images. Med. Image Anal. 1, 109–127.

Khaneja, N., Miller, M.I., Grenander, U., 1998. Dynamic programming generation of curves on brain surfaces. IEEE Trans. Pattern Anal. Mach. Intell. 20, 1260–1265.

Lewis, J.W., Van Essen, D.C., 2000. Mapping of architectonic subdivisions in the macaque monkey, with emphasis on parieto-occipital cortex. J. Comp. Neurol. 428, 79–111.

MacDonald, D., Kabani, N., Avis, D., Evans, A.C., 2000. Automated 3-D extraction of inner and outer surfaces of cerebral cortex from MRI. NeuroImage 12, 340–356.

Meyer, M., Desbrun, M., Schroder, P., Barr, A.H., 2002. Discrete differential-geometry operators for triangulated 2-manifolds. International Workshop on Visualization and Mathematics, VisMath.

Miller, M.I., Massie, A.B., Ratnanather, J.T., Botteron, K.N., Csernansky, J.G., 2000. Bayesian construction of geometrically based cortical thickness metrics. NeuroImage 12, 676–687.

Morland, A.B., Baseler, H.A., Hoffmann, M.B., Sharpe, L.T., Wandell, B.A., 2001. Abnormal retinotopic representation in human visual cortex revealed by fMRI. Acta Psychol. 107, 229–247.

Qiu, A., Bitouk, D., and Miller, M.I. 2005. Smooth functional and structural maps on the neocortex via orthonormal bases of the Laplace–Beltrami operator, submitted to IEEE transactions on medical imaging.

Ratnanather, J.T., Botteron, K.N., Nishino, T., R. and Massie, A.B., Patel, S.G., Peddi, S., Todd, R.D., Miller, M.I., 2001. Validation of cortical analysis of the medial prefrontal cortex. NeuroImage 14, 1058–1069.

Ratnanather, J.T., Barta, P.E., Honeycutt, N.A., Lee, N., Morris, N.G., Dziorny, A.C., Hurdal, M.K., Pearlson, G.D., Miller, M.I., 2003. Dynamic programming generation of boundaries of local coordinatized submanifolds in the neocortex: application to the planum temporale. NeuroImage 20, 359–377.

Ratnanather, J.T., Wang, L., Nebel, M.B., Hosakere, M., Han, X., Csernansky, J.G., Miller, M.I., 2004. Generation and analysis of the cingulate gyrus cortical surface in healthy and schizophrenia subjects. Psychiatry Res. NeuroImaging 132, 53–68.

Robb, R.A., Hanson, D.P., Karwoski, R.A., Larson, A.G., Workman, E.L., Stacy, M.C., 1989. Analyze: a comprehensive, operator-interactive software package for multidimensional medical image display and analysis. Comput. Med. Imaging Graph 13, 433–454.

Schneider, W., Noll, D.C., Cohen, J.D., 1993. Functional topographic mapping of the cortical ribbon in human vision with conventional MRI scanners. Nature 365, 150–153.

Sereno, M.I., Dale, A.M., Reppas, J.B., Kwong, K.K., Belliveau, J.W., Brady, T.J., Rosen, B.R., Tootell, R.B., 1995. Borders of multiple visual areas in humans revealed by functional magnetic resonance imaging. Science 268, 889–893.

Shattuck, D.W., Leahy, R.M., 2001. Automated graph based analysis and correction of cortical volume topology. IEEE Trans. Med. Imag. 20, 1167–1177.

Shattuck, D.W., Sandor-Leahy, S.R., Schaper, K.A., Rottenberg, D.A., Leahy, R., 2001. Magnetic resonance image tissue classification using a partial volume model. NeuroImage 13, 856–876.

Shipp, S., Watson, J.D.G., Frackowiak, R.S.J., Zeki, S., 1995. Retinotopic maps in human prestriate visual cortex: the demarcation of areas V2 and V3. NeuroImage 2, 125–132.

Sunness, J.S., Liu, T., Yantis, S., 2004. Retinotopic mapping of the visual cortex using functional magnetic resonance imaging in a patient with central scotomas from a trophic macular degeneration. Ophthalmology 111, 1595–1598.

Teo, P., Sapiro, G., Wandell, B., 1997. Creating connected representations of cortical gray matter for functional mri visualization. IEEE Trans. Med. Imag. 16, 852–863.

Thompson, P.M., Schwartz, C., Toga, A.W., 1996. High-resolution random mesh algorithms for creating a probabilistic 3D surface atlas of the human brain. NeuroImage 3, 19–34.

Toga, A.W., 1999. Brain Warping. Academic Press, London, UK, pp. 337–363 (Chap. 19).

Tootell, R.G.H., Reppas, J.B., Kwong, K.K., Malach, R., Born, R.T., Brady, T.J., Rosen, B.R., Belliveau, J.W., 1995. Functional analysis of human MT and related visual cortical areas using magnetic resonance imaging. J. Neurosci. 15, 3215–3230.

Tootell, R.B.H., Mendola, J.D., Hadjikhani, N.K., Ledden, P.J., Liu, A.K., Reppas, J.B., Sereno, M.I., Dale, A.M., 1997. Functional analysis of V3A and related areas in human visual cortex. J. Neurosci. 17, 7060–7078.

Van Essen, D.C., Drury, H.A., Joshi, S., Miller, M.I., 1998. Functional and structural mapping of human cerebral cortex: solutions are in the surfaces. Proc. Natl. Acad. Sci. 95, 788–795.

Wahba, G., 1990. Spline models for observational data. SIAM. CBMS-NSF Regional Conference Series in Applied Mathematics, vol. 59..

Warnking, J., Dojat, M., Guerin-Dugue, A., Delon Martin, C., Olympieff, S., Richard, N., Che, A., Segebarth, C., 2002. fMRI retinotopic mapping—Step by step. NeuroImage 17, 1665–1683.

Well 3rd, W.M., Grimson, W.E.L., Kikinis, R., Jolesz, F.A., 1996. Adaptive segmentation of MRI data. IEEE Trans. Med. Imag. 15, 429.

Xu, C., Pham, D.L., Rettmann, M.E., Yu, D.N., Prince, J., 1999. Reconstruction of the human cerebral cortex from magnetic resonance images. IEEE Trans. Med. Imag. 18, 467–479.

Zhang, Y., Brady, M., Smith, S., 2000. A hidden Markov random field model for segmentation of brain MR images. Proc. SPIE Medical Imaging, San Diego, CA. , pp. 1126–1137.

Zhang, Y., Brady, M., Smith, S., 2001a. Segmentation of brain MR images through a hidden Markov random field model and the expectation maximization algorithm. IEEE Trans. Med. Imag. 20, 45–57.

Zhang, Y., Brady, M., Smith, S., 2001b. A statistical framework for automatic brain MR image segmentation. NeuroImage 13, S291.